UHASSELT

KNOWLEDGE IN ACTION

Maastricht University

Faculty of Medicine and Life Sciences
School for Life Sciences

Master of Biomedical Sciences

Masterthesis

Molecular scale insights into initial apatite growth to enhance bone regeneration

Yana De Smet

Thesis presented in fulfillment of the requirements for the degree of Master of Biomedical Sciences, specialization Bioelectronics and Nanotechnology

SUPERVISOR :
Prof. dr. Frank RENNER

SUPERVISOR :
Prof. Dr. techn. Markus VALTINER

MENTOR :
Univ. Ass. Dr. Hsiu-Wei CHENG

Transnational University Limburg is a unique collaboration of two universities in two countries: the University of Hasselt and Maastricht University.

UHASSELT
KNOWLEDGE IN ACTION

2017 2018

UHASSELT
KNOWLEDGE IN ACTION

Maastricht University

Faculty of Medicine and Life Sciences
School for Life Sciences

Master of Biomedical Sciences

Masterthesis

Molecular scale insights into initial apatite growth to enhance bone regeneration

Yana De Smet
Thesis presented in fulfillment of the requirements for the degree of Master of Biomedical Sciences, specialization Bioelectronics and Nanotechnology

SUPERVISOR :
Prof. dr. Frank RENNER
SUPERVISOR :
Prof. Dr. techn. Markus VALTINER

MENTOR :
Univ. Ass. Dr. Hsiu-Wei CHENG

Foreword and acknowledgements

Table of Contents

Glossary

AFM	Atomic force microscopy
$CaCl_2$	Calcium chloride
$CaHPO_4$	Calcium hydrogen phosphate
EDL	Electric double layer
FECO	Fringes of equal chromatic order
HCl	Hydrochloric acid
IHP	Inner Helmholtz plane
Ksp	Solubility product
MBI	Multiple beam interferometry
MD	Molecular dynamics
NaOH	Sodium hydroxide
Na_2HPO_4	Sodium hydrogen phosphate
OHP	Outer Helmholtz plane
PB	Poisson Boltzmann
SFA	Surface forces apparatus
XPS	X-ray photoelectron spectroscopy

Formula abbreviations and parameters:

φ	Surface potential
z	Valence of ions
e	Elementary electron charge
k_B	Boltzmann constant
T	Temperature
ε	Dielectric constant
ε_0	Permittivity of free space
λ_D	Debye length
κ	Inverse of Debye length
c	Molar concentration of ions
N_A	Avogadro constant
n	Refractive index
I	Ionic strength

～ || ～

Abstract

Bone mainly consists of hydroxyapatite ($Ca_{10}(PO_4)_6(OH)_2$) and collagen, giving the bone strength and flexibility. So far, the interplay of hydroxyapatite with body fluids (water, ions and proteins), during the mineralization process, is unclear due to experimental difficulties unraveling dynamic molecular scale effects, *in situ* with high resolution. We hypothesize that the structure of the Electrical Double Layer (EDL) influences the initial growth of apatite, possibly decisively steering nucleation.

For detailed characterization, growth of calcium hydrogen phosphate ($CaHPO_4$) on atomically smooth mica model surfaces was studied as a function of different solution conditions using three approaches: (1) layer-by-layer deposition through dipcoating, (2) *in situ* growth using Atomic Force Microscopy (AFM) and (3) *in situ* growth monitored within the Quartz Crystal Microbalance with Dissipation (QCM-D). The morphology, composition and microscopic characteristics of the minerals were investigated by the Surface Forces Apparatus (SFA), optical microscopy, X-ray Photoelectron Spectroscopy (XPS) and atomic resolution AFM. In addition, a 3D-AFM method was developed to characterize the solid/liquid interface structure in three spatial coordinates before, during and after growth initiation.

Growth of $CaHPO_4$ was initially accompanied by the undesired formation of Calcite ($CaCO_3$) due to presence of environmental carbon dioxide (CO_2). Interestingly, this process was induced by the first surface hydration layer. Specifically, irreversible calcium adsorption leads to charge reversal that can result in local carbonate concentrations above the solubility level, in turn initiating growth. This interesting – but also undesired – result indicates a very strong effect of the EDL on growth initiation, via variation of local concentrations at the surface. Calcite growth is eliminated by environmental control.

Current work on apatite growth indicates similar effects, implying the importance of the EDL on crystal growth initiation. Thus, a better insight into the fundamental phenomena involved in apatite formation may even allow further improvement of osseo-integration and implant stability, via electrolyte control.

Samenvatting

Bot bestaat voornamelijk uit hydroxyapatiet ($Ca_{10}(PO_4)_6(OH)_2$) en collageen, en geeft het bot zijn sterkte en flexibiliteit. Tot op heden, is de wisselwerking van hydroxyapatiet met lichaamsvloeistoffen (water, ionen en proteïnen), tijdens het mineralisatie proces onduidelijk vanwege experimentele moeilijkheden bij het *in situ* ontrafelen van dynamische moleculaire schaaleffecten met hoge resolutie. Wij veronderstellen dat de structuur van de elektrische dubbellaag (EDL) de initiële groei van apatiet beïnvloedt en mogelijk doorslaggevend de nucleatie stuurt.

Voor gedetailleerde karakterisering werd de groei van calciumwaterstoffosfaat ($CaHPO_4$) op atomaire gladde mica modeloppervlakken bestudeerd als een functie van verschillende oplossingen met behulp van drie benaderingen: (1) laag-voor-laag depositie door dipcoating, (2) *in situ* groei met behulp van atoomkrachtmicroscopie (AFM) en (3) *in situ* groei gemonitord met de Quartz Crystal Microbalance with Dissipation (QCM-D). De morfologie, samenstelling en microscopische eigenschappen van de mineralen werden onderzocht via de Surface Forces Apparatus (SFA), optische microscopie, X-ray photoelectron spectroscopy (XPS) en atomische resolutie AFM. Daarnaast, is een 3D-AFM methode ontwikkeld om de vaste/vloeistof interfacestructuur in drie ruimtelijke coördinaten te karakteriseren voor, tijdens en na de start van de groei.

De groei van $CaHPO_4$ ging aanvankelijk gepaard met de ongewenste vorming van calciet ($CaCO_3$) ten gevolge van de aanwezigheid van koolstofdioxide (CO_2) in de omgeving. Interessant is dat dit proces werd geïnduceerd door de eerste hydratielaag op het oppervlak. In meer detail, onmkeerbare calcium adsorptie leidt tot ladingsomkering die kan resulteren in plaatselijke carbonaatconcentraties boven het oplosbaarheidsniveau, die op hun beurt groei initiëren. Dit interessant – maar ook ongeweste – resultaat duidt op een zeer sterk effect van EDL op de groei initiatie, door variatie van locale concentraties op het oppervlakte. Calcietgroei wordt geëlimineerd door omgevingscontrole.

Het huidige werk met betrekking tot apatietgroei geeft vergelijkbare effecten aan, wat het belang van de EDL voor de initiatie van kristalgroei impliceert. Aldus kan een beter inzicht in de fundamentele verschijnselen die betrokken zijn bij apatietvorming zelfs een verdere verbetering van osseo-integratie en implaatstabilitiet mogelijk maken via elektrolytcontrole.

1. <u>Introduction</u>

Bone is a highly specialized supportive connective tissue that exerts several important functions such as locomotion, support and protection of vital organs. Despite its inert appearance it is a highly dynamic organ that is continuously remodeled in order to heal fractures, adapt to mechanical use and balance ion concentrations. Furthermore, bones act as a reservoir of calcium and phosphate resulting in the creation of apatite minerals. The combination of these minerals with collagen results in hydroxyapatite ($Ca_{10}(PO_4)_6(OH)_2$) deposition and is responsible for the typical stiffness and resistance of bone tissue (1). Specifically, the molecular mechanism of growth is central to achieving the structural features and performance specifications that are reached by this fascinating natural material.

1.1   Hydroxyapatite crystallization

The mechanism of the hydroxyapatite crystallization process remains the subject of numerous discussions. However, recent studies show that in solution systems there are already pre-nucleation nanometer-sized structural units present, which are also known as pre-nucleation clusters. Sommerdijk *et al.* have proven that these clusters are calcium triphosphate complexes which progress stepwise to the final composition. The individual phases of the crystallization process were determined according to the calcium/phosphate ratios and are schematically represented in **figure 1**. The pre-nucleation complexes possess an excess of free energy, which fundamentally alters the nucleation pathway. Amorphous phases become accessible at concentrations for which the classical nucleation theory would predict the exclusive formation of the more stable crystalline phases. In other words, the pre-nucleation clusters are shown to lower the energy barrier to initiate nucleation, hereby uniting classical and non-classical nucleation theories (2).
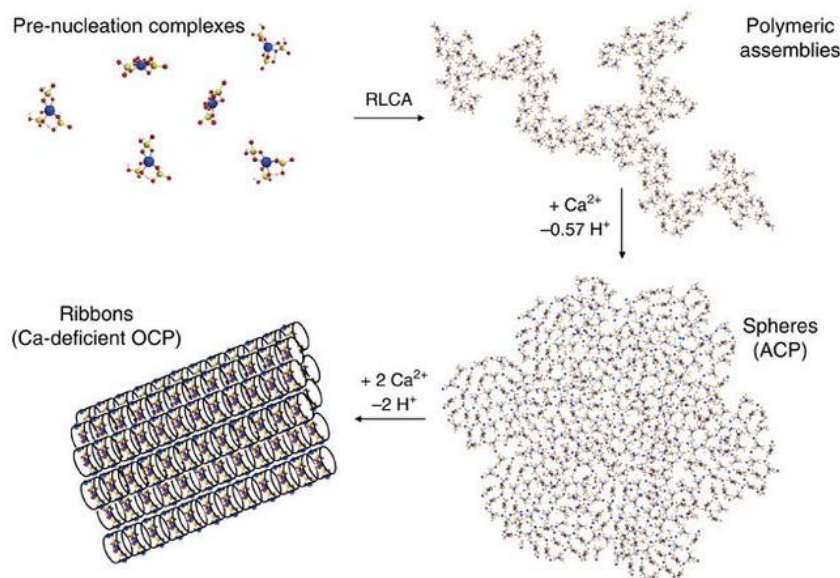
Figure 1: Crystallization mechanism of hydroxyapatite. Pre-nucleation complexes in solution forming branched polymeric assemblies by a reaction-limited aggregation (RLCA) process. Nucleation of amorphous calcium phosphate occurs through the binding of additional calcium ions and the subsequent aggregation of the resulting post-nucleation cluster. This post-nucleation cluster is the basis of the crystal structure of octacalcium phosphate and apatite, which forms through the further uptake of calcium ions.

Until now, the **interplay of body fluids**, more specifically water, ions and proteins, **with the mineralization process has not been investigated due to lack of adequate tools**. Techniques such as atomic force microscopy (AFM) reveal discontinuous step force profiles, leading to the inability to measure the water layers. In an attempt to gain more insight into the detailed structure and behavior of interfacial water layers on the substrate and hydroxyapatite surfaces, molecular dynamic (MD) simulations have been performed. Haihua *et al.* have reported the MD simulated water behavior on ideally perfect crystal faces of hydroxyapatite, showing that two to three well-defined, ice-like organized water layers were formed on the crystal surfaces (3).

However, atomic force microscopy forms the fundamental basis for atomic resolution imaging of substrate phenomena and is able to perform force spectroscopy to provide ion layering information. De Yoreo *et al.* studied *in situ* assembly processes of proteins, peptides and nanoparticles in the design and synthesis of biomimetic materials. They investigated the underlying forces which drive the self-assembly process. In order to do so, AFM-based spectroscopy was combined with AFM high resolution imaging. As a result, ion layering information was provided and could be correlated with the resulting interface phenomena and thus indirectly to the driving forces in the growth process. Two examples of their work are on one hand the investigation of self-assembly of peptoids into nanoribbons on mica surface. Herein, they display that peptoid-mica interactions are stronger than peptoid-peptoid interactions. As a result, the peptoids will self-assemble into discrete nanoparticles, which then transform into hexagonally patterned nanoribbons on the mica surface (4). On the other hand, the crystal growth through nanoparticle assembly was investigated in magnesium chloride and calcium chloride solutions. They found that the attractive interaction driving nanoparticle assembly and orientation result from the coupling between the short-range solution response and the long-range van der Waals interactions. In other words, the orientation and assembly of the particles was associated as a function of the nanometer-scale solvent layers (5). However, the detailed interaction forces of the latter were provided by combining AFM with the surface forces apparatus (SFA).

The surface forces apparatus (SFA) allows control and measurement of surface potentials and interfacial electrochemical reactions with simultaneous measurement of interaction forces and the distance between apposing surfaces (6). Combining SFA with AFM will therefore provide more molecular details about the structure of the electric double layer and its possible effect on the resulting investigated interface phenomena. Recent work on SFA, shows proof of concept on measuring the ion structuring between mica surfaces in several electrolytes. Valtiner *et al.* displayed the effect of water on the layer of interfacial room temperature ionic liquids on substrates such as gold (7). Furthermore, the ion structuring between mica surfaces in caesium chloride and lithium chloride solutions was performed (8).

Here, we aim to measure and visualize the ion structuring of the electrical double layer in calcium chloride and sodium hydrogen phosphate solutions to investigate the EDL's effect on the initial growth of apatite minerals. As the process will be investigated on atomic scale, an atomically smooth model system must be used, a well-known surface with these properties is muscovite mica.

1.2 Model surface for bone growth

The basal plane of muscovite mica ($KAl_2(AlSi_3O_{10})(OH)_2$) has become the classic surface for solid-aqueous interfacial studies and will therefore be used as main substrate. Muscovite mica is a 2:1 clay mineral of which each sheet is composed of three layers (9). The top and bottom layer are formed by tetrahedrons of oxygen with silicon (Si^{4+}) ions in their centers, while the intermediate layer is composed of octahedrons of oxygen with aluminum (Al^{3+}) in their centers. The tetrahedrons share oxygen atoms and hereby form hexagonal rings, in the same way the octahedrons are linked to form octahedral layers (10). The different mica sheets are held together by a single interlayer of potassium (K^+) ions (see **figure 2**). However, the electrostatic binding is relatively weak, resulting in easy cleavage of the mica along the [001] plane. This results in an atomically flat surface over a large surface area (mm²), with chemical uniformity. Furthermore, mica is flexible, has a high shear and tensile strength, is chemically stable and is inert to most liquids (11).

A

B
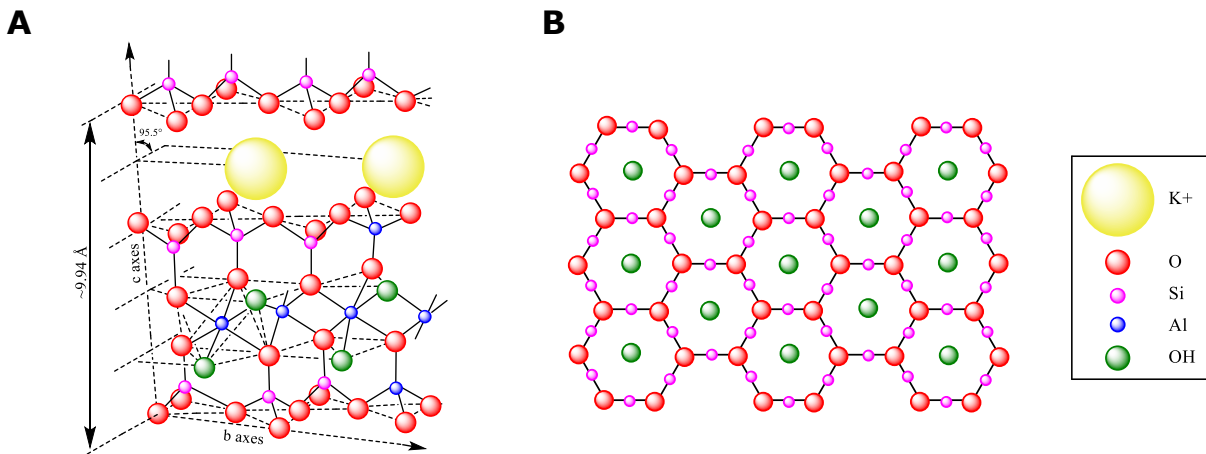
Figure 2: Structure of muscovite mica (**A**) [110] projection (**B**) cleaved surface.

Due to cleaving of the mica surface, the potassium (K^+) ions become exposed on the surface, when immersing the freshly cleaved mica in an electrolyte, charge accumulation and separation will occur at the interface. Hence, the potassium ions will dissociate from the lattice, resulting in a negative surface charge (12). The substrate has the tendency to remain neutral and will, therefore, attract counter ions from the surrounding electrolyte to balance the electric charge density. This redistribution of electrolyte ions results in a layered structure called the electric double layer (EDL).

Since mica is very thin, transparent and atomically smooth sheets can be easily obtained, it is the preferred choice in the monitoring of growth and adsorption processes. De Yoreo *et al.* used mica as a carrier for the growth of apatite minerals (1, 13). Yang *et al.* studied the adsorption of partially hydrolyzed polyacrylamide, an anionic polyelectrolyte, on a mica surface in different environments using atomic force microscopy (14).

1.3 Electric double layer

1.3.1   Theory

In low salt concentrations, the EDL is described according to the Gouy-Chapman-Stern model, and is thus defined as two separate layers. Within the inner Stern layer, the surface charge is partially or sometimes completely balanced by counter ion adsorption (15). The ions in the solution are not able to move in the longitudinal direction of the surface due to adsorbing and Coulomb interactions. If both specific and non-specific adsorption takes place, the layer is further divided into two distinct planes: the inner Helmholtz plane (IHP) and the outer Helmholtz plane (OHP). The IHP passes through the center of the specifically adsorbed ions, also known as the ions that lost their solvation shell, and ranges until the non-specific adsorbing ions on top, while the region between the IHP and the onset of the diffuse layer represents the OHP (see **figure 3**).

In the outer layer, also known as the Gouy-Chapman layer, the excess surface charge is compensated by a Boltzmann distributed layer of oppositely charged ions. This ionic cloud is loosely associated with the surface and consists of free ions that move in the fluid under the influence of electrostatic attraction and thermal motion rather than being firmly anchored (16). Therefore, there is a surface potential decay with the distance perpendicular to the surface. It is therefore also called the diffuse layer. The Stern and Gouy-Chapman layer are referred to as the hydration layers of the substrate (17).
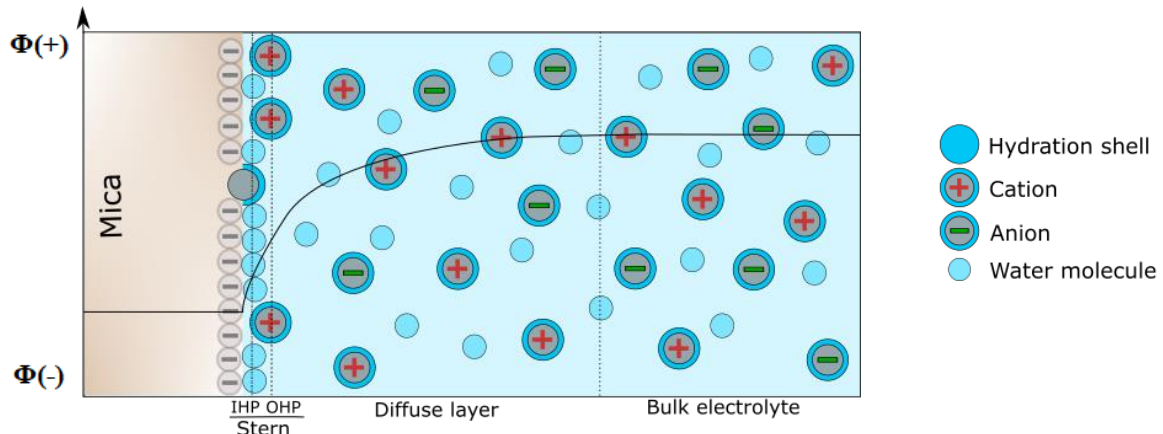
Figure 3: The Gouy-Chapman-Stern model of an electric double layer structure at an isolated charged surface with the corresponding potential distribution over distance.

The thickness of the diffuse layer, also known as the Debye screening length, can be estimated by the Debye Hückel approximation (18):

$$\lambda_D = \frac{1}{\kappa} \qquad \text{(Eq. 1)}$$

With $\quad \kappa = \sqrt{\dfrac{2\,N_A\,I\,e^2\,10^3}{\varepsilon\,\varepsilon_0\,k_B\,T}} \quad$ and $\quad I = \frac{1}{2}\sum_{i=1}^{n} z_i^2\, c_i$

λ_D is the Debye length, N_a is Avogadro's number, I is the ionic strength of the solution, ε the dielectric constant of water, ε_0 the permittivity of free space, k_B the Boltzmann's constant, T the temperature in kelvin, z the valence of the ion and c the concentration of the solution. As can be observed, an increase in the ionic strength will result in a shorter Debye length.

1.3.2   Overcharging

However, this principle is not indefectible, if there are many counterions in the vicinity of the surface in excess of that predicted by the Poisson-Boltzmann approximation, the phenomena known as overcharging or charge reversal will appear. In other words, the charge density of co-ions will exceed the ones of the counterions and will lead to a different distance potential distribution and a charge density of the opposite sign at the Helmholtz plane (19). The main explanation for the overabundance of counterions can be found in the specific adsorption. Charge reversal readily occurs in systems with divalent counterions and is not taken into account in the Poisson-Boltzmann approximation since it neglects the ion-ion correlations and their effect on the EDL structure (20).

1.4   Research objectives and strategy

As already mentioned above, the major aim of this research is to see whether and how the electric double layer effects the initial growth of apatite. For this purpose, the growth of apatite was simplified to the biomimetic precipitation of calcium hydrogen phosphate (CaHPO4) on atomically smooth muscovite mica and silicon dioxide (SiO_2) sensors. In particular, we have investigated the effect of the electrolyte composition; pH and surface potential on the microscopic and macroscopic characteristics of the resulting mineral deposits on the surfaces. The objective is to gain a more detailed molecular level understanding of the interplay between water, ions and surface charge mediated interface structuring in electrolyte concentrations and its influence on interfacial forces and surface reactivity.

The strategy to gain more insight into the molecular scale is the combination of layer-by-layer growth through dipcoating, *in situ* growth in the atomic force microscope and monitoring of the *in situ* growth in the Quartz crystal microbalance with dissipation. **These analysis techniques provide morphological, structural and chemical information allowing visualization of the electric double layer and the resulting precipitants.** Furthermore, the electric double layer was dissected in three dimensions by developing an innovative 3D-AFM technique, which allows atomic resolution imaging and force spectroscopy simultaneously. The technique and its analysis will be further elaborated in the results section. Besides these main techniques, other supporting methodologies were used such as surface forces apparatus (SFA) and X-ray photoelectron spectroscopy (XPS).

The project can be divided in four subsections of which the first one focuses on the preconditioning of the electric double layer. Secondly, we have used different calcium chloride concentrations and investigated their interaction with the mica surface. Thirdly, we have monitored the growth of calcium hydrogen phosphate in function of deposition cycles and concentrations. Lastly, the extended description of the three dimensional AFM method and the corresponding analysis.

2. <u>Material and methods</u>

2.1 Chemicals

Acetone (Rectapur, assay >99.5%), ammonia (NH_3, 25%), hydrochloric acid (HCl, 5N), hydrogen peroxide (H_2O_2, 30%) and technical grade sodium hydroxide (NaOH) were purchased from VWR. Calcium chloride (purity 99+%), calcium hydrogen phosphate dihydrat (purity 98+%), magnesium chloride hexahydrat (purity 99+%) and di-sodium hydrogen phosphate (purity 99+%, anhydrous) were obtained from Carl Roth. Deionized water was obtained from a Milli-Q system. All chemicals were used without further purification.

2.2 Dipcoating

The most widely used method to fabricate thin films for industrial and laboratory applications is layer-by-layer growth through dipcoating, since it is easy, fast, has a low cost and a high coating quality and high degree of control. This growth method consists of alternate immersions in suspensions of opposite charge with wash steps in between; resulting in multilayer films deposited a layer at a time. The technique is an electrostatically driven self-assembly procedure which is self-limiting in adsorption of the individual layers through electrostatic repulsion.

The substrate is immersed in a solution of the coating material at a constant speed and remains there for a well determined amount of time. Subsequently, a coherent liquid film is entrained on withdrawal of the substrate at a constant speed since the solution naturally and homogeneously spreads out on the substrate surface by the combined effects of viscous drag and capillary rise. Excess liquid will drain from the surface and evaporation will take over to lead to solidification of the film on the substrate (see **figure 4**). This process is repeated until the desired film specifications are reached. Many factors influence the final state of the film: initial substrate surface, submersion time, withdrawal speed, number of dipping cycles, solution composition and concentration, and the environmental temperature, vapor pressure and humidity. Therefore, a fine tuning of the deposit conditions is necessary to perfectly control the film characteristics (thickness, roughness and structure) (21).

In this project, two different immersion solutions were used: calcium chloride ($CaCl_2$) and sodium hydrogen phosphate (Na_2HPO_4). The sample was left in the solution for 30 seconds and subsequently withdrawn at a constant speed. Between the dipping in the different solutions, the samples were rinsed with MiliQ-water.
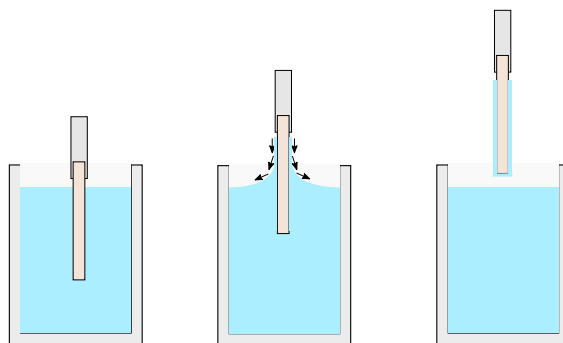

Figure 4: The fundamental stages of dipcoating. The arrows indicate the liquid flow.

2.3 Atomic force microscopy

2.3.1   General principle

Atomic force microscopy (AFM) is a surface analytical technique, belonging to the family of scanning probe microscopy, which generates very high-resolution topographic images of a surface down to molecular/atomic resolution. The core principle of AFM is based on measuring the forces between a sharp probe (<10nm) and a surface at a very short distance (0.2-10nm). The sharp probe, also referred to as tip, is attached to a cantilever and scans the sample surface. A laser beam is pointed on the cantilever and reflects back into a detector. When the tip approaches the sample surface, interaction forces will attract or repel the tip, resulting in a slight change in the direction of the reflected beam, which is detected by the position-sensitive photo diode (PSPD, see **figure 5**). The alteration in deflection is subsequently translated into the surface image by the use of Hooke's law (22):

$$F = k . x \qquad (Eq. 2)$$

Figure 5: schematic of an atomic force microscope with optical detection of the defection of the microcantilever.

In general, the distance between the AFM tip and the surface is kept constant by a feedback parameter which depends on the imaging mode used. The parameter is predetermined by the operator and corresponds via Hooke's law to the amount of force that the cantilever exerts on the sample. In other words, the operator is able to control the amount of force being applied to the sample surface while imaging (23). While scanning the surface, the feedback parameter is sensed and compared to the desired value, if they are different, the feedback amplifier will apply a voltage to the piezo to raise or lower the sample relative to the cantilever to restore the desired value. The voltage that the feedback amplifier applies to the piezo is therefore a measure of the height of features on the sample surface and is displayed as a function of the lateral position of the sample.

Here, an Asylum Research Cypher AFM with the implemented bluedrive™ option was used. Bluedrive improves tapping mode techniques by replacing the conventional drive mechanism with photothermal excitation. In short, a second laser additional to the usual deflection sensing laser beam is focused onto the base of the cantilever. The power of the laser is modulated causing localized heating of the cantilever, causing it to bend and oscillate at the modulation frequency. The laser only excites the cantilever and no other mechanical components in the AFM, generating a very clean and stable cantilever response in both air and liquids, also enabling driving cantilevers in very viscous fluids like ionic liquids.
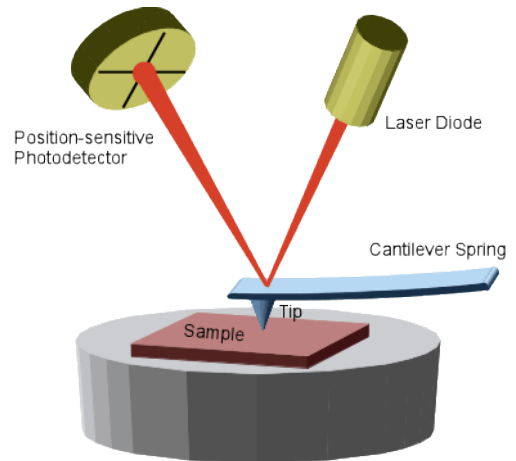
2.3.2   Operational modes

The AFM can be operated into several modes: contact mode, non-contact mode and tapping mode. In this project, both contact mode and tapping mode were used. Contact mode, also known as Constant Force or Deflection Feedback Mode, operates by raster scanning the surface with a probe tip in constant physical contact. The tip deflects the lever as it moves over the surface topography. The operator is able to control the amount of force being applied to the sample surface while imaging, a higher set-point voltage will result in increasing the imaging force while reducing the set-point will result in reduced imaging forces and thus a more gentle interaction between tip and sample. One of the drawbacks of this mode is the exerted lateral force on the sample in the direction of travel. This force can be quite high and result in sample damage or removal of relatively loosely attached objects. The measurements were performed with a gold coated ContGB-G tip with a cantilever length of about 450 µm, spring constant of 0.2 N/m and a resonant frequency of 13 kHz.

On the other hand, tapping mode, also referred to as intermittent contact mode or amplitude modulation AFM, operates by a small piezo in the cantilever holder that causes the cantilever to oscillate with high amplitude at or near its resonant frequency. The frequency and amplitude of the driving signal are kept constant as long as there is no drift or interaction with the surface. When the tip is near the surface, several interaction forces such as Van der Waals and dipole-dipole interactions will occur and cause the amplitude of the cantilever's oscillation to change as the tip gets closer to the sample. The oscillation amplitude of the tip is measured by the detector and the tip-sample separation is adjusted through the feedback loop to maintain constant amplitude and force on the sample. In contrast to the contact mode, a lower set-point value will result in a higher force exerted on the sample surface.

Tapping mode prevents the tip from sticking to the surface and causing damage during scanning. The surface material is not pulled sideways since the applied force is always vertical and thus the issue of lateral forces and drag across the surface is avoided. However, one of the drawbacks within this mode is the drift that arises due to temperature changes and/or fluid levels in liquids. The measurements were performed with an arrow-UHF-AuD tip with a cantilever length of about 35 µm, an unspecified spring constant and a resonance frequency in the range of 0.7-2MHz.

2.3.3   Force spectroscopy

Force spectroscopy is a single point measurement technique in which the cantilever approaches the sample and after interaction withdraws again. During this measurement, the deflection is measured as function of the piezo movement, which can be converted to force as function of the tip-sample separation to provide mechanical information about the sample and in this work, ion structuring in the electrical double layer. A model force curve can be observed in **figure 6**.
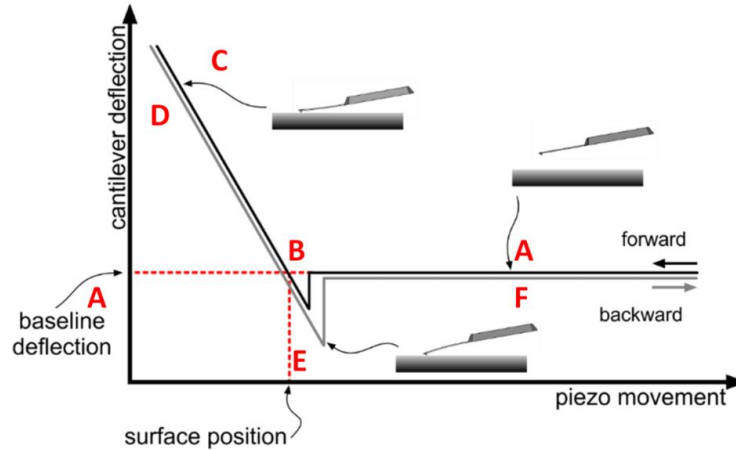
Figure 6: Schematic diagram of a typical AFM force-distance curve. Figure adapted from nanosurf company.

The force curve can be divided in multiple segments where the black line refers to motion of tip approaching the surface and the gray line the retraction. During the approach, the available attractive or repulsive forces between the tip and the sample can be measured by bending of the cantilever (A). At a certain point, the cantilever will snap-in to contact with the sample due to tip-surface interactions like capillary forces (B). The tip and sample stay in contact and the cantilever keeps bending due to further movement of the z-piezo (C). In section D, withdrawal of the tip from the surface will occur, leading to the unbending of the tip. The tip will undergo an adhesive dip before it is able to emerge from the adhesion of the interface (E) and will subsequently return to its unperturbed state while the Z-piezo further increases the tip-sample distance (F).

2.4   Surface forces apparatus

The surface forces apparatus (SFA) instrument uses a similar approach to AFM to measure the interaction forces between two materials. In contrast to AFM, the SFA is more suited to measure the surface-surface interactions and long range forces. Furthermore, the technique is able to determine the separation distance between the two surfaces with sub-nanometer resolution, which is made possible due to the use of interferometry.

The general SFA setup is based on two cylindrically curved glass discs on which transparent surfaces such as mica are mounted. The cylindrical axes of the discs are positioned at 90° to each other and approach each other normal to the axes. One of the surfaces is held by a cantilevered spring and the deflection of the spring is used to calculate the force being exerted. Furthermore, position measurements are performed with multiple beam interferometry (MBI), therefore, the mica surfaces are back coated with a thin layer of high reflectivity material e.g. silver to give them a mirror function while still transmitting some light (24).

Subsequently, white light is directed through the surfaces and will reflect and forth until the point of closest contact between the two surfaces is reached and a set of wavelengths is transmitted and detected by the spectrometer (**figure 7**). The resulting interference pattern is known as fringes of equal chromatic order (FECO) and allows distance determination between the two surfaces. The transmitted light can also create Newton rings, which can be visually observed through a

microscope objective. Furthermore, the SFA is not only limited to longitudinal movement. Lateral movement is also enabled and allows the detection of shear force between the two surfaces.

In general, SFA allows high resolution force-distance profiles between apposing surfaces. Hereby, it is possible to measure the thickness of a deposited calcium hydrogen phosphate layer on a mica surface with nanometer-accuracy (25).
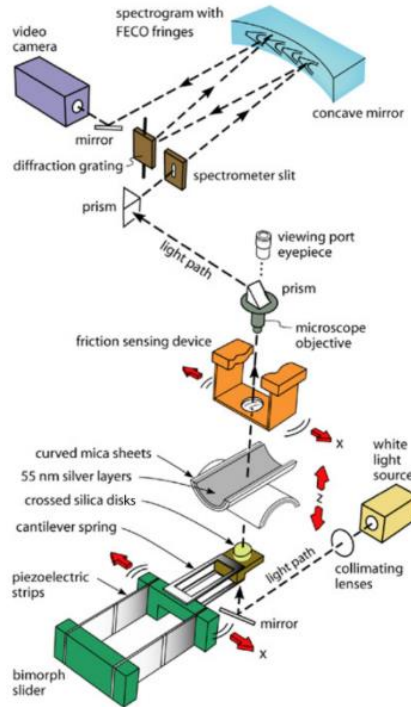

Figure 7: Schematic of SFA setup showing the light path in a typical experiment. Figure adapted from (26).

2.5 Quartz crystal microbalance with dissipation

Quartz crystal microbalance with dissipation (QCM-D) is an acoustic surface sensitive technique that is based on acoustic waves generated by oscillating a piezoelectric, single crystal quartz plate to measure mass and viscoelastic properties of a layer on top of a QCM-D sensor. The piezoelectric quartz crystal of the QCM-D is located between two gold electrodes and exhibits the converse piezoelectric effect. Thus, by applying an alternating electric field over the electrodes, an alternating expansion and contraction of the crystal lattice will be induced.

When a sufficient AC voltage is applied, with a frequency close to the resonant frequency (f_0) of the quartz crystal, the quartz will start to oscillate at its acoustic resonance frequency. A transverse acoustic wave thus propagates across the crystal, reflecting back into the crystal at the surface. When the acoustic wavelength is equal to twice the combined thickness of the crystal (t_q) and electrodes, a standing wave can be established. Hence, the resonance frequency is related to the thickness of the crystal and is given by (27):

$$f_0 = \frac{v_0}{2t_q}$$
(Eq. 3)

Where v_q is the velocity of the acoustic wave in AT cut quartz (3.34×104 m/sec), f_0 is the resonance frequency of the quartz crystal prior to the mass change and t_q is the thickness of the

quartz. The QCM-D estimates a mass per unit area, meaning that the change in frequency of the oscillating crystal is related to the mass adsorbed on the quartz surface. This linear relationship between frequency change (Δf) and mass adsorbed (Δm) was proposed by Sauerbrey in 1959:

$$\Delta m = \frac{c}{n}\Delta f \qquad \text{(Eq. 4)}$$

Where n is the harmonic number and

$$C = \frac{t_q \rho_q}{f_0}$$

with t_q the thickness of quartz, and ρ_q the density of quartz. When the AC voltage is turned off, the oscillation amplitude decays exponentially, this decay is recorded and the frequency (f) and the energy dissipation factor (D) of different overtones are extracted. The decay rate is related to the elasticity and viscosity of the molecular layer on the sensor. The dissipation D is the ratio between the dissipated energy during one vibration cycle and the total kinetic and potential energy of the crystal at that moment.

$$D = \frac{E_{lost}}{2\pi E_{stored}} \qquad \text{(Eq. 5)}$$

where E_{lost} is the energy lost during one oscillation cycle and E_{stored} is the total energy stored in the oscillator.

In this projects, the QCM-D was used on a Q-sense E1 instrument (Gothernburg, Sweden) that monitors the shift in frequency (Δf) and dissipation (ΔD). The shift in Δf and ΔD was monitored at six different overtones (3rd to 11th) of which the 7th was used for data analysis. The Q-sense E1 allows to fixate the temperature between 15 and 50°C. All the measurements were performed by using AT-cut quartz crystals with SiO_2 coating (diameter 14 mm, thickness 0.3 mm, surface roughness 3 mm and resonant frequency 4.95 MHz).

After the usage, the sensors were cleaned according to the RCA 2 protocol. At first, the RCA 2 protocol was established by performing a 6:1:1 mixture of MiliQ-water (conductivity of 0.055 Scm^{-1} at 25°C), hydrochloric acid and hydrogen peroxide. The sensors were thoroughly rinsed and subsequently blown dry with nitrogen gas.
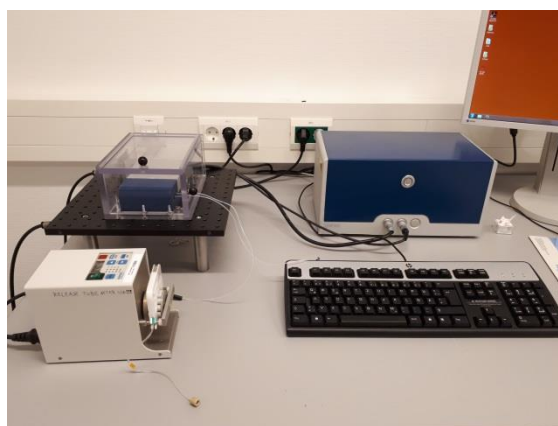

Figure 8: The QCM-D set-up.

2.6 Optical microscope

A nanofocus µsurf explorer, a 3D confocal microscope, was used for precision 3D measurement and analysis of surfaces. Providing information of topography, layer thickness and roughness in the micrometer and nanometer range. The objective lens offers individual measurement field sizes between 1.6 mm x 1.6 mm and 260 µm x 260 µm with freely selectable vertical resolution. The objective lenses are from Olympus and provide a 20x and 100x magnification.

2.7 X-ray photoelectron spectroscopy

XPS measurements were performed with a fully automated Quanterra 2 (Düsseldorf, Germany, Physical Elecronics). All XPS spectra were measured with the "high-power mode" of the used machine. In this mode photoelectrons are generated by continuously scanning a 100×100 µm^2 sized X-ray spot (100 W) over an area of 100×1000 µm^2 in order to minimize X-ray damage to the sample. All data were recorded with a pass-energy of 26.00 eV, and a spectral resolution of 0.1 eV. To obtain a good signal-to-noise ratio 3 sweeps for the Au 4f signal, and 20-30 sweeps for all other signal were used. All RTIL XPS samples were prepared in a glove bag filled with dry Argon atmosphere and expose to humidity for less than 2-3 minutes during XPS introduction.

3. <u>Results and discussion</u>

3.1   Electrical double layer preconditioning

The first step in determining the influence of the electrical double layer on the crystallization process of apatite minerals is the investigation of the interaction between the mica surface and the resulting minerals. In more detail, if the minerals have the ability to grow directly on the mica surface. Otherwise, the mica substrate will only function as a carrier for the precipitated minerals.

3.1.1   Mica-mineral interaction

A freshly cleaved mica surface was placed underneath an optical microscope set-up. A droplet mixture of 100 mM calcium chloride (pH 5) and 19 mM sodium hydrogen phosphate (pH 8) was deposited on top of the mica surface. During mixture, an immediate formation of crystals occurred in the solution, however, after rinsing with miliQwater and blow drying with nitrogen gas, no microscopic structures could be observed anymore (see **figure 9B**). Therefore, a different strategy was applied; a different mica substrate was alternately immersed in the 100 mM calcium chloride (pH 5) and 19 mM sodium hydrogen phosphate (pH 8) solution at a constant speed. The substrate was left in each solution for approximately 30 seconds. After five cycles of deposition; the substrate was rinsed with miliQwater and blown dry with nitrogen gas. As can be seen in **figure 9C**, the substrate clearly displays the formation of a porous structure, more specifically calcium hydrogen phosphate.
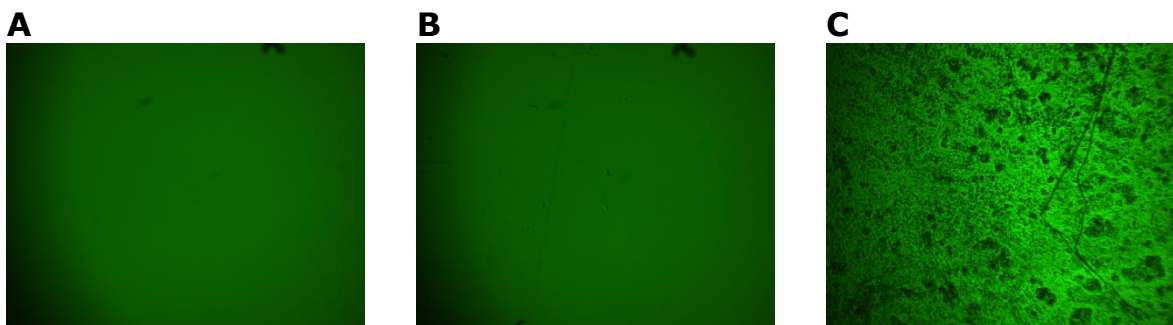
A   **B**   **C**

Figure 9: Comparison of the mica surface topography by optical microscopy (**A**) after cleavage, (**B**) after exposure of the surface to a 100 mM $CaCl_2$ (pH 5) and 19 mM Na_2HPO_4 (pH 8) mixture and (**C**) after dipcoating the mica surface alternately in the same $CaCl_2$ and Na_2HPO_4 solutions. All three samples were rinsed with MiliQWater and dried with nitrogen.

Even though sample B didn't display any microscopic features underneath the objective, this doesn't mean that there is nothing deposited on the surface. A more in depth investigation of the surface topography was performed by in contact mode imaging with the atomic force microscopy in air. The surface scan displayed the coverage of the mica surface with calcium hydrogen phosphate (see **figure 10**). However, the mixing of the solutions leads to in solution growth, which is also deposited on the mica surfaces and leads to the deposit of bigger crystals. To get a better control over the thickness and roughness of the deposited mineral layer, it is therefore recommended to use the dipcoat mechanism in which the different solutions are alternately flown through at a certain flow rate.
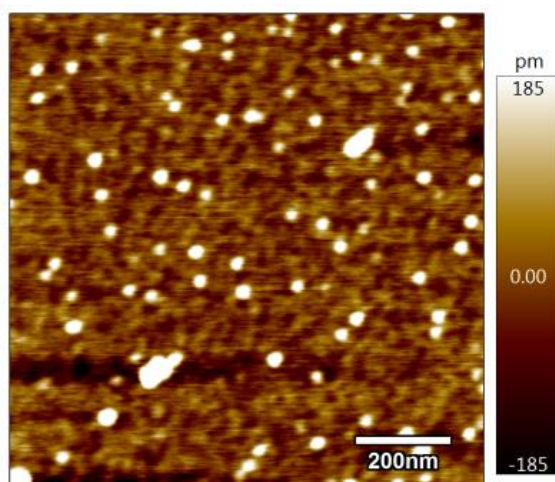
Figure 10: Contact mode AFM topography scan of mica surface after dipcoating in a mixture of 100mM $CaCl_2$ and 19mM Na_2HPO_4 for 5 cycles, 1μm x 1 μm.

The mica surface allows direct growth of minerals independent if the deposition method is in solution growth or a layer-by-layer deposit through dipcoating. Although the dipcoat mechanism is recommended for a better growth control in order to study the initial growth on a molecular scale in a stepwise manner.

3.1.2 Calcite growth

The dipcoat mechanism was replicated in the AFM set-up by placing a freshly cleaved mica surface inside and flowing through a solution of 100 mM calcium chloride of pH 5. The expected outcome of this experiment was the visualization of calcium ion absorption on the mica lattice, but instead a crystallization process occurred without any addition of sodium hydrogen phosphate (**figure 11**).
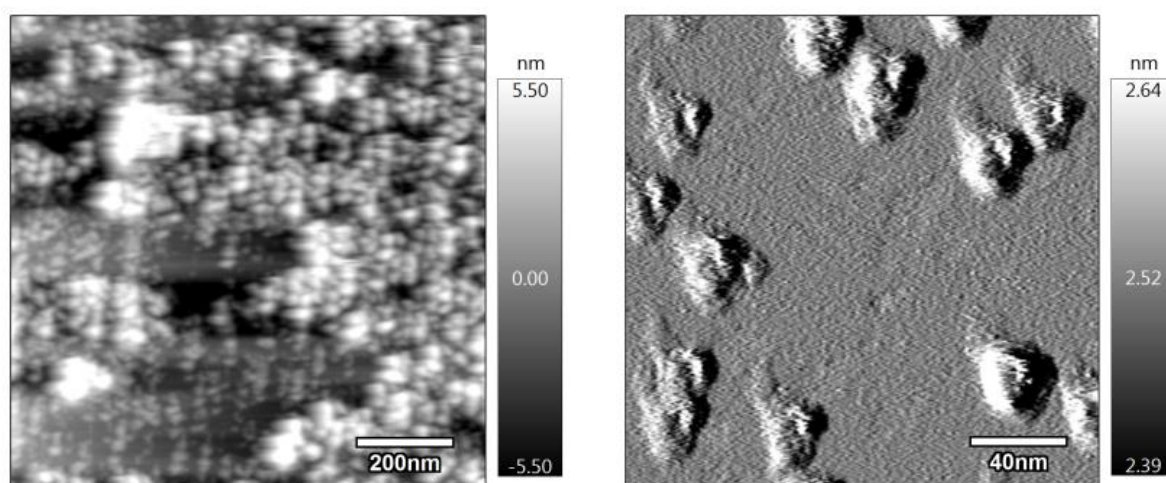

Figure 11: AM-AFM scans in aqueous 100 mM CaCl2 solution (pH 5) displaying the early precipitation of calcite on a mica surface, 1 μm x 1μm.

In order to investigate the composition of the deposited crystals, the samples were sent for XPS. As can be seen in the XPS spectra (**figure 12**), the results indicate the presence of calcium carbonate (calcite). The intensity signal is rather low, but is explainable by the sample process. The sample was covered in a calcium chloride solution and blown dry with a low flow of nitrogen gas, leading to drying out of the calcium chloride on the surface, creating a rather thick layer on top of the calcite crystals, leading to a diminishment of the signal intensity.
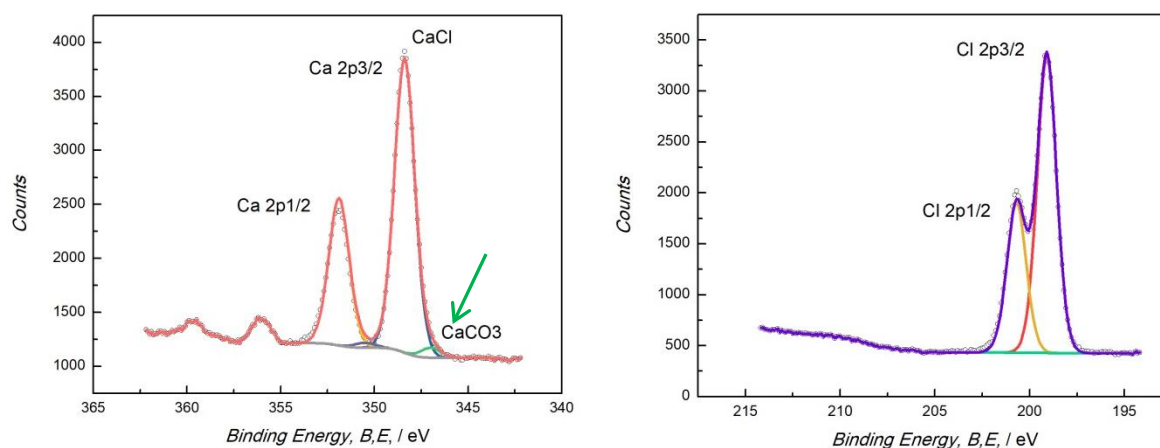

Figure 12: Fitted small spot X-ray photoelectron spectroscopy (XPS) spectra of Ca 2p and Cl 2p signals from an N2 blow-dried mica surface which wetted by CaCl2 solution previously.

However, calcite crystallization should not occur in these conditions. Literature indicates that at these conditions with a 100 mM calcium chloride solution of pH 5 and an environmental concentration of 400 ppm carbon dioxide, calcite crystallization should not occur, since the concentration of carbonate would be 10^{-11}. Based on our calculations (**Eq. 6**), which include the solubility product, the carbonate concentration would be 3.36×10^{-8} and thus a power of three bigger than the expected value in solution. So why would there be any carbonate precipitation?

$$[CO_3^{2-}] = \frac{[Ca^{2+}]}{K_{sp}}$$ (Eq. 6)

With $[Ca^{2+}]$ = 0.1 M and Ksp = 3.36×10^{-9} M

The only explanation for this crystallization to occur is the effect of the electrical double layer as follows. The counterion density near the surface is known to be largely dependent of the surface charge. In other words, the first hydration layer has an increase in ion concentration of the opposite and thus the counterion profile in a solution of 10^{-4} M over the first few angstroms can reach concentrations up to a 0.1 M equivalents of a bulk solution. This also means that we may find a potential local concentration increase of ions at the interface of mica. However, mica is naturally negatively charged (see again in the introduction). As a consequence, the concentration of cations would increase. Here we see precipitation of calcite and what this needs is a positive charge on mica. How is this possible?

In order to achieve a concentration increase of carbonate, a positive overcharge must necessarily occur on mica, making it thermodynamically favorable for calcite crystallization to occur. We can now speculate that the calcium ions in solution may adsorb at the lattice places which are

available. In turn this will clearly lead to a so-called overcharging with an effectively high positive surface charge that is caused by adsorption of ions. As such, we already see here, that ions in solution (in this case Ca^{2+}) do have a strong influence on growth of crystalline phases. Here we observe an unwanted side product growth. But this may already suggest a general principle, in accordance with the expectation of this work. Indeed, we may already conclude that double layer structures have a great influence on growth processes.

As calcite is totally undesired in the growth process of calcium hydrogen phosphate or any form of apatite mineral, the presence of carbonate must be eliminated by environmental control. Thus, indicating that pretreatment of the mica and solution, and thus preconditioning of the electrical double layer is necessary to avoid undesired calcite formation. Control experiments with degassed solutions indicated no further calcite growth. In the remaining part of this work, only degassed solutions were used.

The first hydration layer of the electric double layer increases the ion concentration with a power of three compared to the bulk electrolyte, leading to an overcharge. As a result, the undesired calcite crystallization occurs in a calcium chloride solution due to the environmental carbon dioxide. Pretreatment of the electric double layer is therefore necessary by controlling environmental conditions.

3.2 Monolayer of calcium ions adsorption on mica

To understand the influence of the electrical double layer in the growth process with the dipcoat mechanism, the first step need to be studied in more detail, meaning that the interaction between the calcium chloride solution and the mica surface needs to be studied separately. It is now interesting to see, if indeed calcium ions condensate into the mica lattice, leading to the expected overcharging, that initiated calcite growth as discussed above.

Therefore, the initial bare mica surface was imaged in air by contact mode AFM, the substrate is flat and featureless (**figure 13**). In order to eliminate interfering noise signals and possible scanning artifacts, the image of the mica lattice was Fourier filtered. The obtained image shows a hexagonal pattern, which corresponds to the theoretical lattice dimensions (**figure 2**). The hydroxide ions are invisible on the surface, since these atoms are lying underneath the top-lattice layer.
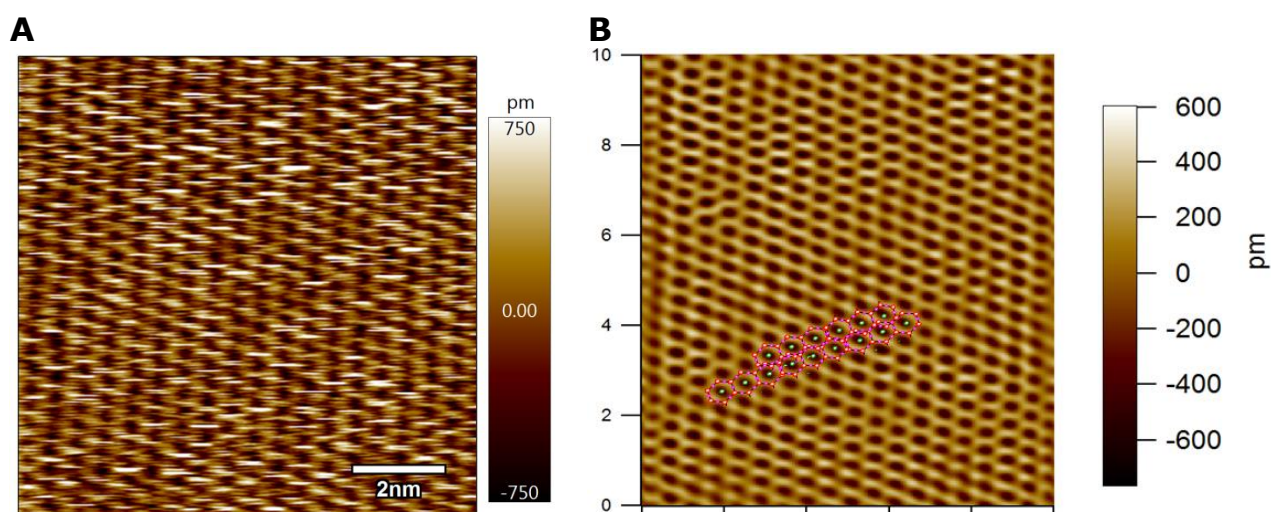

Figure 13: Mica lattice structure. (**A**) Lattice structure imaged by contact mode AFM in air (**B**) the corresponding Fourier filtered image with the theoretical hexagonal lattice overlay, 10 nm x 10 nm.

Subsequently, *in situ* adsorption experiments were conducted under stagnant aqueous-phase conditions. The calcium chloride solution was pretreated by purging with argon and sonicated to eliminate environmental carbon dioxide and thus the early precipitation of calcite. By immersing the mica surface in the aqueous solution, the potassium and sodium ions will dissociate. The surface will acquire a negative charge, which may induce strong adosprtion of calcium ions. Indeed, in **figure 14**, we can clearly see atomically resolved condensation of calcium ions into the hexagonal lattice of mica. This provides a visual atomic scale prove that mica is indeed overcharging in a calcium chloride solution. This again emphasizes how an ion in solution changes the surface properties in solution dramatically. Here we do see a complete charge reversal.
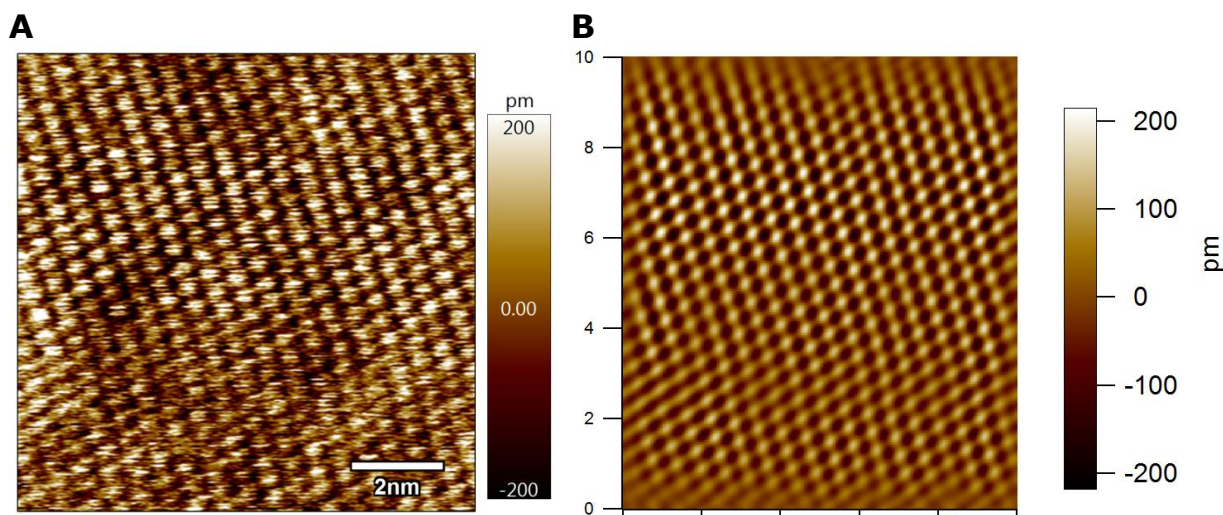
Figure 14: (**A**) a monolayer of absorbed calcium ions on muscovite mica surface imaged in AM-AFM (**B**) the corresponding Fourier filtered image, 10 nm x 10 nm.

The adsorption of calcium on the mica lattice was further investigated by performing QCM-D measurements of adding different calcium chloride concentrations with washing steps in between (see **figure 15**). The resulting frequency changes upon addition of calcium chloride indicated the adsorption of calcium on the mica surface and confirmed the previous result. However, when rinsing the sample with miliQwater, the frequency signal did not return to the original baseline, indicating that even **irreversible calcium adsorption occurs**. Furthermore, the QCM-D data was converted to the mass on the sensor by using the Sauerbrey equation. In general, calcium ions have an atomic radius of 2.31 Å leading to a surface area of 16.76 Å². However, when correcting for the close packing of equal spheres on the surface, this leads to a total area of 12.41 Å² per calcium ion in a monolayer.

In **figure 15A**, a clear frequency shift of 3.2 Hz is observed when adding 20 mM of calcium chloride of pH 7. According to the Sauerbrey mass conversion, this corresponds to an areal mass of 55.529 ng/cm², and thus an area of 12 Å² per calcium ion. The measured area per calcium ion is smaller than the theoretical one and thus indicates the presence of an overcharge on the surface. Furthermore, when applying the same strategy for calcium chloride concentrations of 100 mM and 300 mM of pH 7, the area per calcium ion decreases even more to 6.37 Å², and 2.33 Å² per calcium ion. The comparison between these data therefore indicates that a concentration of approximately 20 mM leads to a **monolayer coverage of calcium ions on the sensor surface**, meaning that **figure 14** also represents a monolayer on the mica lattice.
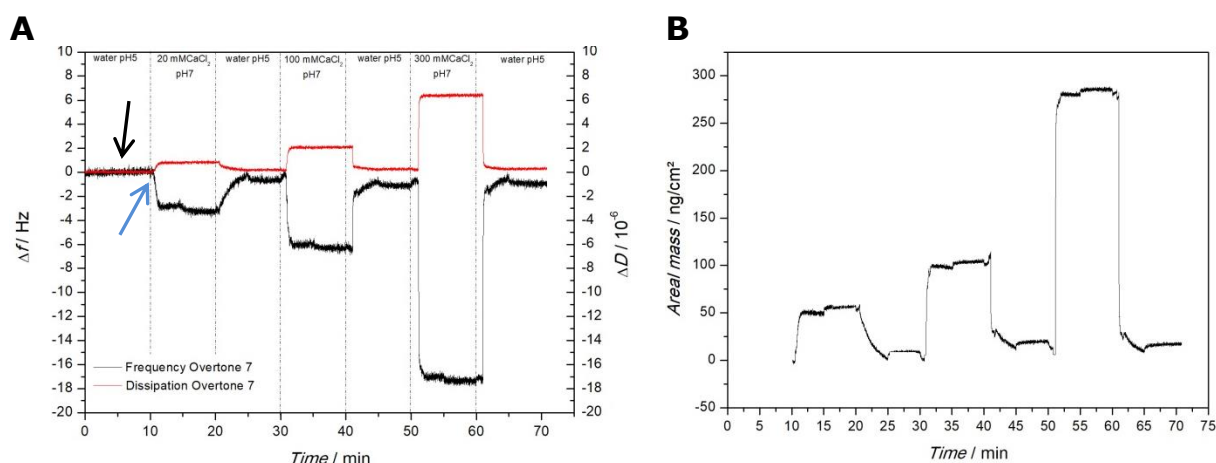
Figure 15: Δf and ΔD for the 7th overtone as a function of time upon calcium absorption. (**A**) The stepwise growth of calcium hydrogen phosphate by alternately flowing through 20 mM calcium chloride pH 7, miliQwater and 19 mM sodium hydrogen phosphate pH 8. The black arrow indicates the stable baseline created by addition of MiliQWater. The blue arrow indicates the point of addition of the calcium chloride solution, which induces a drop in frequency. (**B**) is the conversion of the frequency shift to the mass in function of time.

The mica surface with the calcium adsorption was subsequently rinsed with a sodium hydroxide solution. In the end, the sample was rinsed with miliQwater and blown dry with nitrogen gas. The XPS spectra indicate the presence of calcium on the surface, confirming previous statements regarding the **irreversible calcium adsorption on mica lattice**. The silicon and aluminum signal present in the XPS spectrum are from the mica lattice.
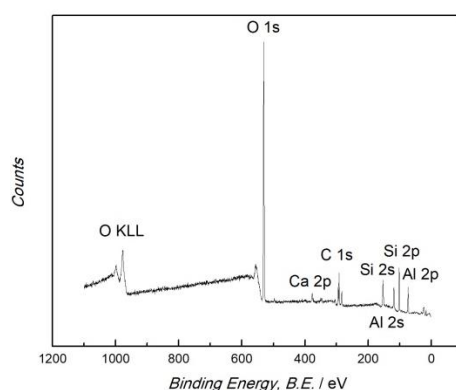
Figure 16: small spot X-ray photoelectron spectroscopy (XPS) spectrum of Ca 2p signals from an N$_2$ blow-dried mica surface that was exposed to 100 mM of calcium chloride pH 7.

Pretreating of the electric double layer no longer displays the calcite crystallization but the irreversible adsorption of calcium ions on the mica lattice. The irreversible adsorption of calcium was both confirmed by the unreturning baseline of the QCM-D and the XPS result, which displays the remainder of calcium on the surface after rinsing and blow drying the surface. Furthermore, the calcium chloride concentration of 20 mM seems to represent the boundary of the formation of a monolayer or overcharge on the surface.

3.3 Growth process of CaHPO$_4$

To grow the main component of the apatite minerals, calcium hydrogen phosphate, two different approaches were used: layer-by-layer growth through dipcoating and *in situ* growth monitored within the Quartz crystal microbalance with dissipation. The latter mechanism was performed by flowing through calcium chloride, miliQwater and sodium hydrogen phosphate solutions in an alternating method with a constant speed of 0.5 mL/min. Each solution was flown through for a period of 5 minutes before changing to the next one. Within the resulting graphs, one can observe that the signal has a delay of one minute upon changing the solution; this delay is due to the injection tube length. After performing five deposition cycles of 20 mM calcium chloride (pH 7) and 19 mM sodium hydrogen phosphate, a clear shift in frequency can be observed (see **figure 17**). The frequency shift is converted to the areal mass by using the Sauerbrey equation and displays a stepwise increase in mass, indicating surface growth.
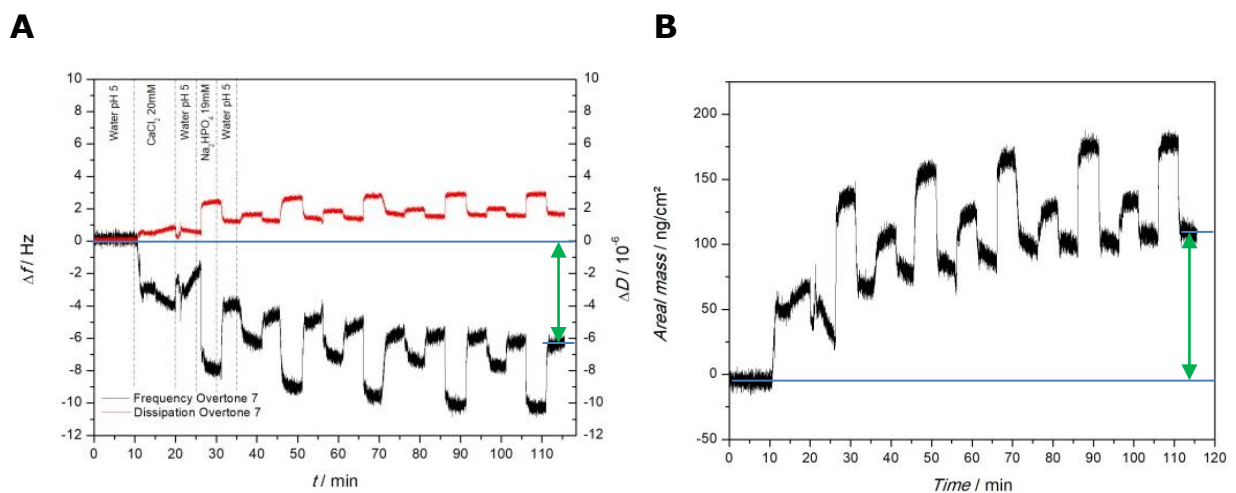
A   **B**

Figure 17: (A) Δf and ΔD for the 7th overtone as a function of time upon calcium hydrogen phosphate growth by alternating the flow through of 20 mM CaCl2 pH7, MiliQWater and 19 mM Na2HPO4. (B) The frequency shift converted to the areal mass in function of time. The green arrow indicates the frequency, and thus mass, change between the pre and post deposition of calcium hydrogen phosphate.

Performing this growth experiment with a varying calcium chloride concentration of 20 mM, 100 mM and 300 mM of pH 7 with a fixed concentration of 19 mM sodium hydrogen phosphate, allows establishment of mass in function of number of cycles curves for the different concentrations (**figure 18**). As can be observed for all three concentrations, the areal mass on the sensor increases linearly with the increase in the number of deposit cycles. However, among the different calcium chloride concentrations, a clear trend can be observed. **The 20 mM experiment displays a higher increase in mass compared to the higher concentrations**. One would expect it to be the other way around, since more ions are available for performing growth. However, the experiments are performed in a stepwise way in flow. The high concentration of calcium ions leads to a lot of **electrostatic repulsion between the ions**, leading to less irreversible adsorption on the surface. As a result, when rinsing with miliQwater in the next step, a lot of calcium ions are washed away. The lack of these calcium ions on the surface therefore lead to a lower growth rate when flowing through the phosphate solution.
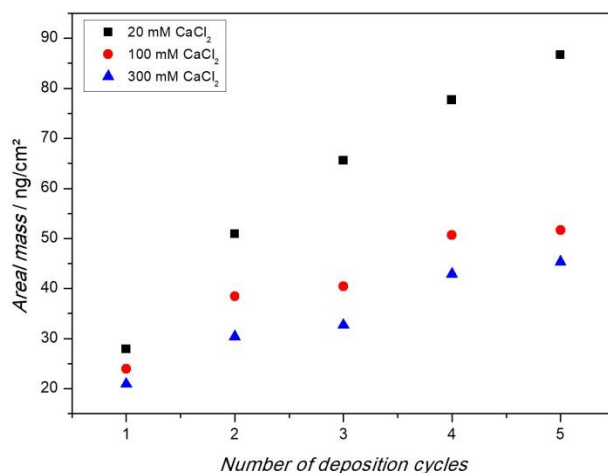
Figure 18: Areal mass of CaHPO4 in function of the number of cycles for different concentrations of calcium chloride.

As confirmation of the structure composition on the surface, the samples were send to XPS and compared to a reference sample (**figure 19**). The reference contained calcium hydrogen phosphate powder which was fixed on carbon tape. The sample displayed the same composition and atomic ratios as the reference sample, and thus confirms the growth of calcium hydrogen phosphate on the surface.

A

B
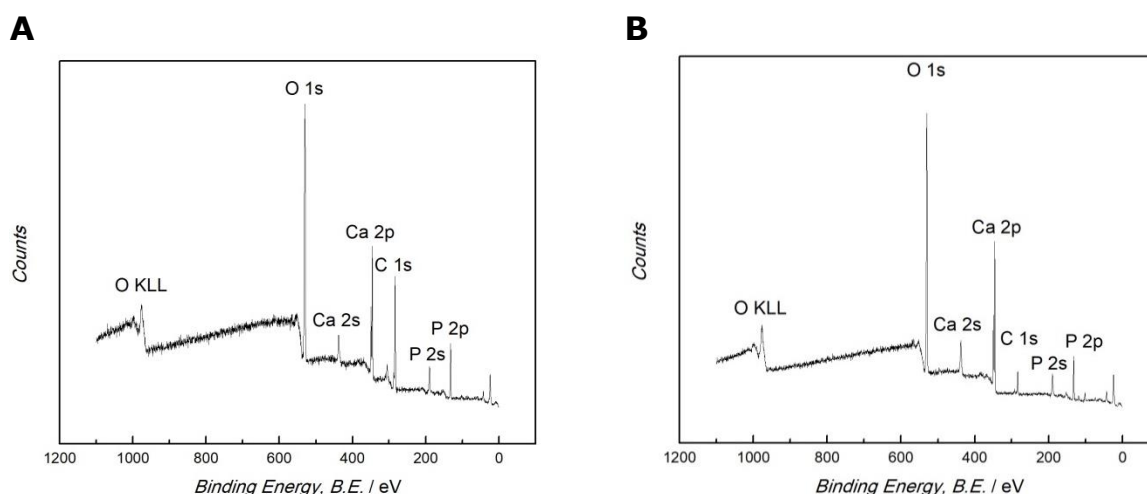
Figure 19: small spot X-ray photoelectron spectroscopy (XPS) spectrum of Ca 2p and P 2p signals from (A) a reference calcium hydrogen phosphate powder on a carbon tape surface and (B) an N2 blow-dried mica surface that was exposed to 100 mM of calcium chloride pH 7 and 19 mM of sodium hydrogen phosphate pH8.

The next step is to control the growth extent of the calcium hydrogen phosphate and more specifically the thickness of the deposited layers. An important factor to influence the film layer thickness is the withdrawal speed at which the dipcoating is performed. Two mica substrates were dipped in a solution of 100 mM CaCl2 pH 7 and subsequently in 19 mM of sodium hydrogen phosphate. However, one sample was withdrawn at a speed of 18 mm/sec while the other one had a withdrawal speed of 1.8 mm/sec. In the end, both samples were rinsed with miliQwater and blown dry with nitrogen gas so that they could be imaged with the confocal microscope and by contact mode AFM in air (**figure 20**).

The sample with the **faster withdrawal speed had bigger features** on both the micrometer as the nanometer scale (**figure 20 A, C**). Also the general roughness of the surface was higher and there was a thicker layer deposit than the slower sample (**figure 20 E, F**). This is due to the fact that a faster withdrawal speed pulls up more fluid onto the surface of the substrate before it has time to flow back down into the solution. By the excess of fluid upon the surface, more ions are available to induce growth and lead to bigger structures.
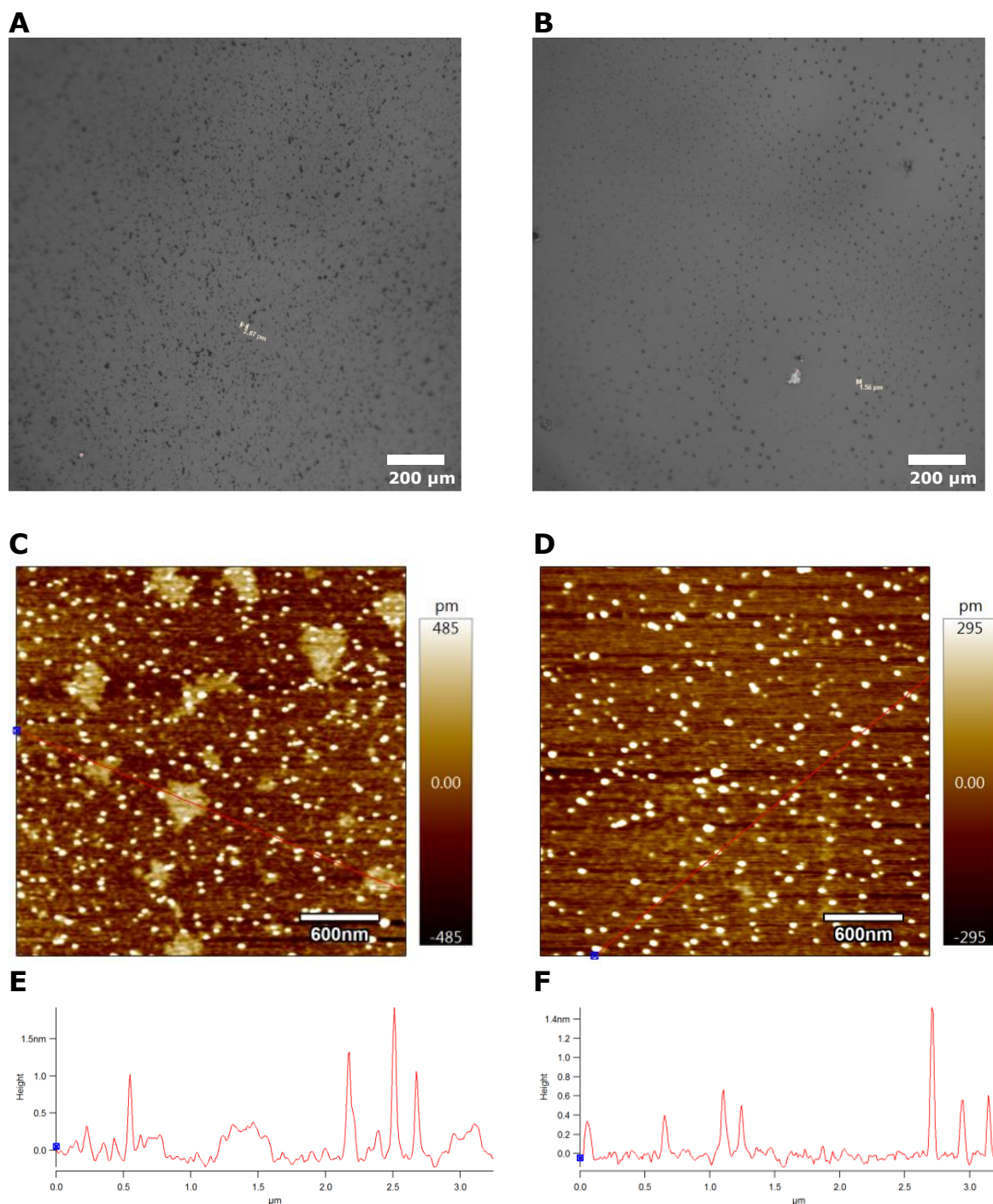
Figure 20: The influence of withdrawal speed during dipcoating. A single cycle of calcium hydrogen phosphate growth was performed on muscovite mica and imaged in air with a confocal microscope **(A)** and **(B)** and by AM-AFM **(C)** and **(D)**. Surface topography after withdrawal speed of **(A,C)** 18 mm/sec and **(B,D)** 1,8 mm/sec. Both samples were rinsed with miliQwater and dried with N2 before imaging, 3 μm x 3 μm, with **(E)** and **(F)** being the corresponding cross-section height profiles.

However, the AFM can only provide roughness information and not the exact thickness of the deposited layer, since the entire surface is covered and there is no possibility from the AFM to know where the actual mica surface is. Therefore, the SFA was used to determine the thickness of the deposited layer with nanometer precision. An SFA disc with the reflective mica was dipcoated alternately in a solution of 100 mM $CaCl_2$ pH 7 and 19 mM Na_2HPO_4 pH 8. In total, five deposition cycles were performed and the sample was rinsed with miliQwater and finally blown dry with nitrogen gas. The sample was placed in the SFA set-up and brought into contact with the apposing smooth mica surface, leading to the creation of a newton ring (**figure 21**).
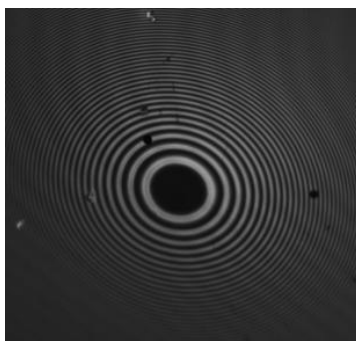

Figure 21: Newton ring of the adhesive contact in air between two apposing mica surfaces.

The cross-view of this newton ring results in the fringes of equal chromatic order. First of all, a dry contact is made, between two uncoated mica surfaces as a reference (**figure 22A**). Subsequently, one of the surfaces gets the dipcoat procedure and a new contact is made. According to the alteration and displacement of the FECO, the distance of the deposited layer on the mica substrate can be calculated. However, **the sample is birefringent and leads to much distorted FECO**, making it complicated to determine the thickness (**figure 22B**). As a solution, a **refractive index matching oil of 1.6160 was used to fill up the air holes in the porous structure**, leading to nice FECO (**figure 22C**). The thickness of the calcium hydrogen phosphate sample was determined on 1.471 μm after five cycles of deposition.

A   **B**   **C**
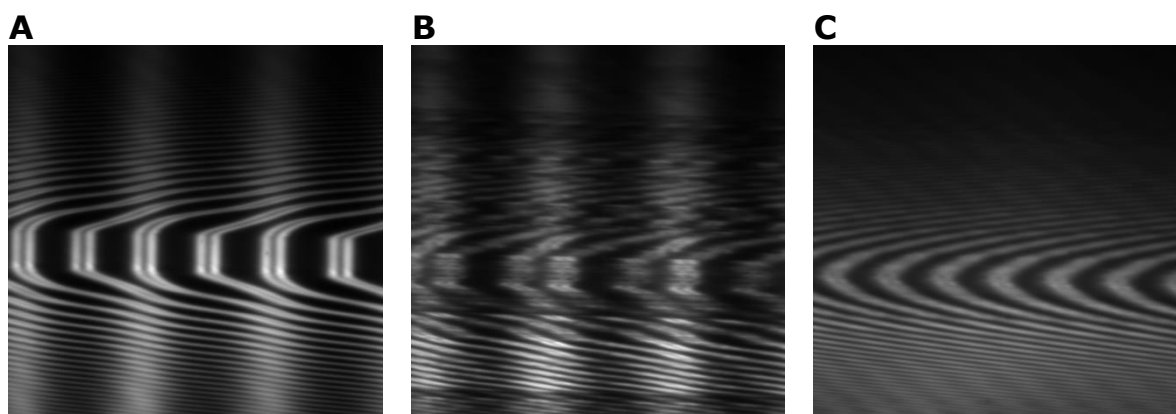
Figure 22: FECO fringes corresponding to (a) adhesive contact in air, (b) after five cycles of dipcoating with 100 mM $CaCl_2$ pH 7 and 19 mM Na_2HPO_4, (c) after addition of refractive index matching oil (RI: 1,6160).

The growth of calcium hydrogen phosphate was established. A clear trend could be observed for the different concentrations of calcium chloride, leading to more growth with a smaller concentration and an increased number of deposition cycles. The withdrawal speed during dipcoating has a significant influence on the roughness of the samples and the growth control. Furthermore, the refractive index matching oils resolved the birefringence allowing thickness determination.

3.4 3D-AFM

As previously mentioned, calcium chloride concentrations higher than 20 mM lead to overadsorption of calcium ions on the mica structure. As a result, ion structuring within the electric double layer in the Z direction arises. However, with normal AFM scanning this layering cannot be observed, only a visual assumption of multiple layers can be made according to the unit cell dimensions (**figure 23**). Bigger scan sizes even create the presumption of the presence of holes in the layering on the mica surface (**figure 23 B, C**). It is rather not clear if these "holes" represent an underlying layer of calcium ions adsorbed on the surface lattice or represent the mica lattice itself and thus no surface coverage. In order to determine the ion and water structuring on the interface, a combination of normal XY AFM imaging and force spectroscopy was made, also referred to as three-dimensional atomic force microscopy.

A

B

C
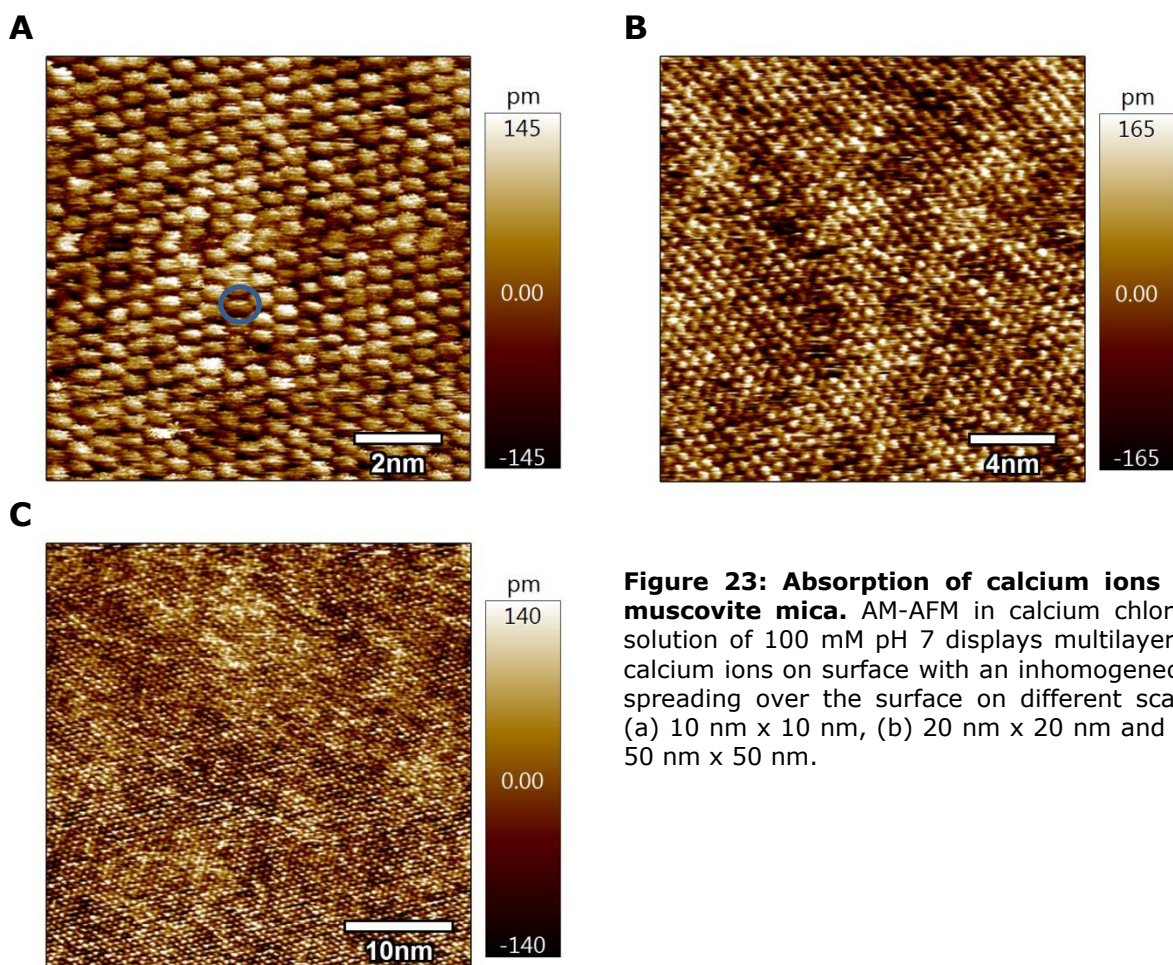
Figure 23: Absorption of calcium ions on muscovite mica. AM-AFM in calcium chloride solution of 100 mM pH 7 displays multilayer of calcium ions on surface with an inhomogeneous spreading over the surface on different scales (a) 10 nm x 10 nm, (b) 20 nm x 20 nm and (c) 50 nm x 50 nm.

As the name implies, 3D-AFM is a method to characterize the structure of a solid/liquid interface in three spatical coordinates, leading to atomically resolved images with information of the layering. The measurement is performed by running XY scanning in tapping mode and at the same time adding a ramping voltage to the z piezo. In this way, for each scanning point, a force distance curve is performed. The external input signal is applied to the AFM, before amplification to high voltage, with an external labview card. The Zsensor is the actual signal in the AFM, remarkable is that the signal is the inverse of the applied signal (**figure 24**).

As a testing system, a mica surface was placed in the AFM and covered with a stagnant aqueous solution of 300 mM calcium chloride (pH 3). The resulting images lead to a combination of XY and Z data. In order to analyze this, a python analysis script was written (**see SI**). **Figure 24A** displays the force curve, more specifically and inrun, in one of the imaging points. Herein, the cantilever moves from far away of the surface to the surface. This signal displays the signal that was added to the AFM and thus the movement of the cantilever in the Z range in function of time.

The z sensor signal for this force curve was plotted against the external input signal and displays an almost linear line (**figure 24B**). This result indicates that the small peaks that are visible in the input signal, is low noise interference. Eventually the amplitude change was plotted in function of the linear fit of the user input signal, leading to change in amplitude signal over the Z range motion, with each peak indicating poking through an ion layer, **the number of peaks therefore indicates the number of layers on the solid/liquid interface.** The amplitude alteration can be converted into 2D cross-sections in XZ direction to give a visualization of the ion structuring on a surface, hereby providing elucidation of the electrical double layer structure.
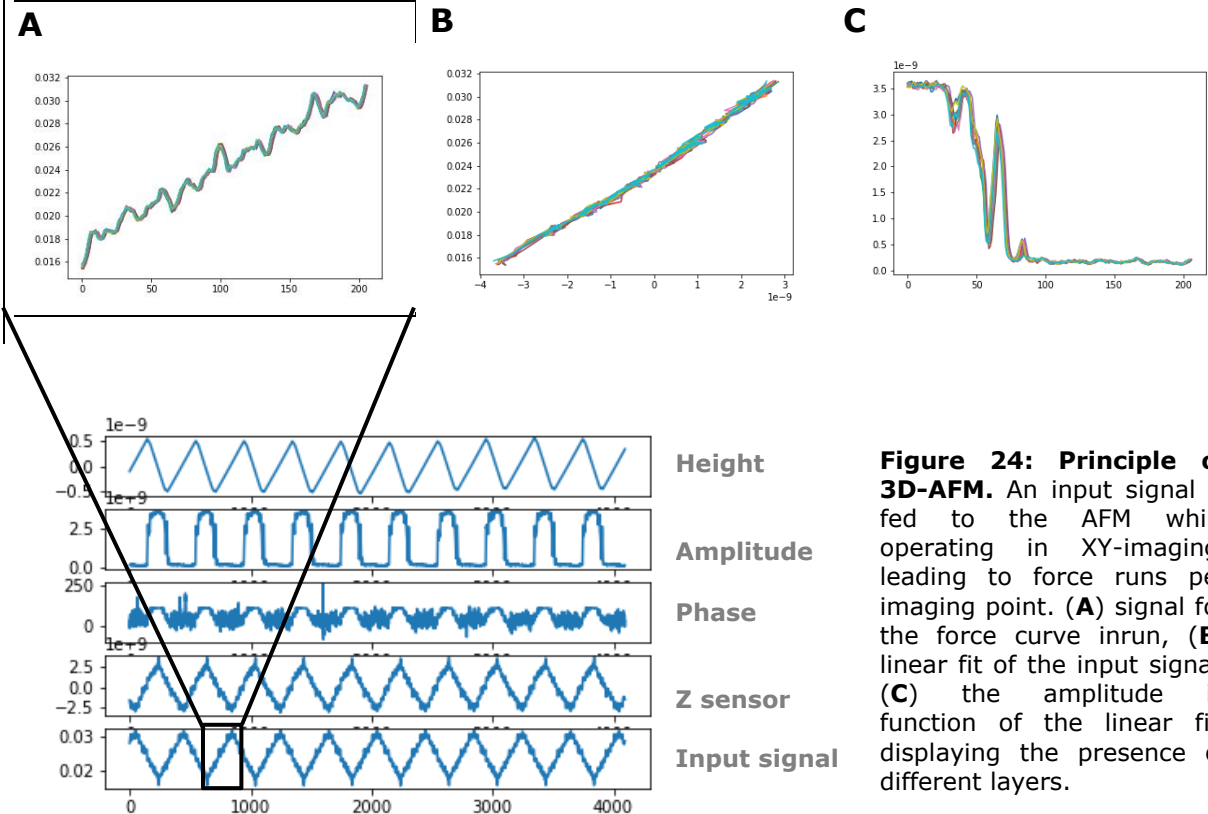
Figure 24: Principle of 3D-AFM. An input signal is fed to the AFM while operating in XY-imaging, leading to force runs per imaging point. (**A**) signal for the force curve inrun, (**B**) linear fit of the input signal, (**C**) the amplitude in function of the linear fit, displaying the presence of different layers.

The 3D-AFM is a method that enables the determination of the force-distance curve on each point of the scanning area on the surface. In the first testing experiment, transition peaks are observed in the amplitude signals, indicating the presence of ion layering. Further analysis and development of the technique is necessary to draw more conclusions out of this data.

4. <u>Conclusion and outlook</u>

This master thesis project was carried to examine the influence of the electrical double layer on the biomimetic precipitation of calcium hydrogen phosphate using AFM, QCM-D and dipcoating as main experimental techniques. The interfacial phenomena on the mica and silicon dioxide surfaces were studied and correlated to the electric double layer structuring. Subsequently, these results were brought into relation with the apatite growth. The main findings are as followed:

First of all, the first hydration layer of the electric double layer increases the ion concentration with a power of three compared to the bulk electrolyte. Hereby, introducing undesired calcite crystallization due to the presence of environmental carbon dioxide. Pretreatment of the EDL resolved the issue.

Secondly, calcium ions are irreversible adsorbed on both the mica as the silicon dioxide surface. The calcium chloride concentration of 20 mM seems to represent the theoretical border at which monolayer formation on the surface switches to overcharging. The overadsorption of the calcium ion can be visualized by applying the three dimensional AFM. The method, displays the transitions between different layers in solution, but needs further analysis.

Lastly, the actual growth of calcium hydrogen phosphate was established and displayed a clear relationship regarding the calcium chloride concentration and the number of deposition cycles. A higher calcium concentration leads to less growth due to the electrostatic repulsion between ions. Also the withdrawal speed in the dipcoating process has an important role regarding the roughness of the deposited layer and the growth rate at which it occurs. A slower withdrawal speed, correlates to a better growth control.

In short we can conclude that the electric double layer does have a significant influence on the crystallization of apatite minerals. However, further measurements are necessary to draw stronger conclusions. Follow-up experiments would exist out of tracking down the importance of the deposition sequence and the first calcium deposition. Possibly the EDL only adsorbs a specific amount of calcium independent of the bulk concentration, hereby limiting the growth process in the first step. Furthermore, hydration layer forces are believed to have an influence on the adsorption of biomolecules such as collagen, surface active proteins, and sugars. The influence of these molecules on the apatite growth is of significant importance. In the long run, expanding the model system and understanding the phenomena involved in apatite formation could lead to the design of advanced metal implants with a focus on enhanced osseo-integration and long-term stability.

5. References

1.   Habraken WJEM, Tao J, Brylka LJ, Friedrich H, Bertinetti L, Schenk AS, et al. Ion-association complexes unite classical and non-classical theories for the biomimetic nucleation of calcium phosphate. Nature Communications. 2013;4:1507.
2.   Florencio-Silva R, Sasso GRdS, Sasso-Cerri E, Sim, #xf5, es MJ, et al. Biology of Bone Tissue: Structure, Function, and Factors That Influence Bone Cells. BioMed research international. 2015;2015:17.
3.   Pan H, Tao J, Wu T, Tang R. Molecular simulation of water behaviors on crystal faces of hydroxyapatite. Frontiers of Chemistry in China. 2007;2(2):156-63.
4.   Chen C-L, Zuckermann RN, DeYoreo JJ. Surface-Directed Assembly of Sequence-Defined Synthetic Polymers into Networks of Hexagonally Patterned Nanoribbons with Controlled Functionalities. ACS nano. 2016;10(5):5314-20.
5.   Li D, Chun J, Xiao D, Zhou W, Cai H, Zhang L, et al. Trends in mica-mica adhesion reflect the influence of molecular details on long-range dispersion forces underlying aggregation and coalignment. Proceedings of the National Academy of Sciences of the United States of America. 2017;114(29):7537-42.
6.   Valtiner M, Banquy X, Kristiansen K, Greene GW, Israelachvili JN. The Electrochemical Surface Forces Apparatus: The Effect of Surface Roughness, Electrostatic Surface Potentials, and Anodic Oxide Growth on Interaction Forces, and Friction between Dissimilar Surfaces in Aqueous Solutions. Langmuir : the ACS journal of surfaces and colloids. 2012;28(36):13080-93.
7.   Hsiu-Wei C, Philipp S, Boaz M, Theodoros B, Xavier B, Uwe RF, et al. Characterizing the Influence of Water on Charging and Layering at Electrified Ionic-Liquid/Solid Interfaces. Advanced Materials Interfaces. 2015;2(12):1500159.
8.   Baimpos T, Shrestha BR, Raman S, Valtiner M. Effect of interfacial ion structuring on range and magnitude of electric double layer, hydration, and adhesive interactions between mica surfaces in 0.05-3 M Li(+) and Cs(+) electrolyte solutions. Langmuir : the ACS journal of surfaces and colloids. 2014;30(15):4322-32.
9.   Classification and structures of the micas. Reviews in Mineralogy and Geochemistry. 1984;13(1):1-12.
10.   Bhattacharyya KG. XPS study of mica surfaces. Journal of Electron Spectroscopy and Related Phenomena. 1993;63(3):289-306.
11.   Crystal chemistry of the true micas. Reviews in Mineralogy and Geochemistry. 1984;13(1):13-60.
12.   Vatti AK, Todorova M, Neugebauer J. Ab Initio Determined Phase Diagram of Clean and Solvated Muscovite Mica Surfaces. Langmuir : the ACS journal of surfaces and colloids. 2016;32(4):1027-33.
13.   De Yoreo JJ. A holistic view of nucleation and self-assembly. MRS Bulletin. 2017;42(7):525-36.
14.   Zhao F, Du Y-K, Tang Ja, Li X-C, Yang P. Morphology of adsorption anionic polyelectrolytes to mica substrate in different environment visualized by atomic force microscopy. Colloids and Surfaces A: Physicochemical and Engineering Aspects. 2005;252(2):153-6.
15.   Otto S. ZUR THEORIE DER ELEKTROLYTISCHEN DOPPELSCHICHT. Zeitschrift für Elektrochemie und angewandte physikalische Chemie. 1924;30(21-22):508-16.
16.   Gouy M. Sur la constitution de la charge électrique à la surface d'un électrolyte. J Phys Theor Appl. 1910;9(1):457-68.
17.   Israelachvili JN. Chapter 14 - Electrostatic Forces between Surfaces in Liquids. Intermolecular and Surface Forces (Third Edition). San Diego: Academic Press; 2011. p. 291-340.
18.   The Electric Double Layer. Physics and Chemistry of Interfaces.
19.   García-Giménez E, Alcaraz A, Aguilella V. Overcharging Below the Nanoscale: Multivalent Cations Reverse the Ion Selectivity of a Biological Channel2010. 021912 p.

20.   Pashley RM. DLVO and hydration forces between mica surfaces in Li+, Na+, K+, and Cs+ electrolyte solutions: A correlation of double-layer and hydration forces with surface cation exchange properties. Journal of Colloid and Interface Science. 1981;83(2):531-46.

21.   Puetz J, Aegerter MA. Dip Coating Technique. In: Aegerter MA, Mennig M, editors. Sol-Gel Technologies for Glass Producers and Users. Boston, MA: Springer US; 2004. p. 37-48.

22.   Binnig G, Quate CF, Gerber C. Atomic force microscope. Physical review letters. 1986;56(9):930-3.

23.   Miller EJ, Trewby W, Farokh Payam A, Piantanida L, Cafolla C, Voïtchovsky K. Sub-nanometer Resolution Imaging with Amplitude-modulation Atomic Force Microscopy in Liquid. Journal of Visualized Experiments : JoVE. 2016(118):54924.

24.   Israelachvili JN. Thin film studies using multiple-beam interferometry. Journal of Colloid and Interface Science. 1973;44(2):259-72.

25.   Israelachvili J. Interferometric Method for determining Refractive Index and Thickness of Thin Films. Nature Physical Science. 1971;229:85.

26.   Israelachvili J, Min Y, Akbulut M, Alig A, Carver G, Greene W, et al. Recent advances in the surface forces apparatus (SFA) technique. Reports on Progress in Physics. 2010;73(3):036601.

27.   Ferreira GN, da-Silva AC, Tome B. Acoustic wave biosensors: physical models and biological applications of quartz crystal microbalance. Trends in biotechnology. 2009;27(12):689-97.

6. <u>Supplementary Information</u>

6.1 Python script for 3D-AFM analysis

```python
from tkinter import Tk
from tkinter.filedialog import askopenfilename
from tkinter import *
import numpy as np
from igor.binarywave import load
import scipy as scy
from scipy import stats
import matplotlib.pyplot as plt
import peakutils as put
from sklearn.linear_model import LinearRegression

Tk().withdraw()
file = askopenfilename(filetypes = [("ibw files","*.ibw")])
print(file)

data = load(file)
dataarray = data['wave']['wData']
print(dataarray.shape)

print(data['wave']['labels'])

plt.figure(1)
plt.subplot(511)
plt.plot(dataarray[:,0,0]) #height
plt.subplot(512)
plt.plot(dataarray[:,0,1]) #amplitude
plt.subplot(513)
plt.plot(dataarray[:,0,2]) #phase
plt.subplot(514)
plt.plot(dataarray[:,0,3]) #zsensor
plt.subplot(515)
plt.plot(dataarray[:,0,4]) #userinput
print(dataarray[:,0,0], dataarray[:,0,0].shape)
print(dataarray[0,:,0], dataarray[0,:,0].shape)
print(dataarray[0,0,:], dataarray[0,0,:].shape)
plt.savefig('overall_signals.png')
plt.show()
```

```python
## finding the minimal and maximal points in the graph ##
maxima = put.indexes(dataarray[:,0,3], thres = 0.5, min_dist = 300)
print(maxima, maxima.shape)


minima = put.indexes(-dataarray[:,0,3], thres = 0.5, min_dist = 300)
print(minima, minima.shape)


## plotting the datapoints between the maxima and minima for every parameter ##
for cuva in range(0, maxima.shape[0]):
    inruns1 = dataarray[maxima[cuva]:minima[cuva+1],0,1] #amplitude
    plt.plot(inruns1)
plt.savefig("amplitude_overall.png")
plt.show()


for cuva in range(0, maxima.shape[0]):
    inruns2 = dataarray[maxima[cuva]:minima[cuva+1],0,2] #phase
    plt.plot(inruns2)
plt.savefig("phase_overall.png")
plt.show()


for cuva in range(0, maxima.shape[0]):
    inruns = dataarray[maxima[cuva]:minima[cuva+1],0,3] #zsensor
    plt.plot(inruns)
plt.savefig("zsensor_overall.png")
plt.show()


for cuva in range(0, maxima.shape[0]):
    inruns3 = dataarray[maxima[cuva]:minima[cuva+1],0,4] #userinput
    plt.plot(inruns3)
plt.savefig("input_overall.png")
plt.show()


##plotting of data against eachother ##
for cuva in range(0,maxima.shape[0]):
    inruns = dataarray[maxima[cuva]:minima[cuva+1],0,3]
    inruns1 = dataarray[maxima[cuva]:minima[cuva+1],0,1]
    plt.plot(-inruns, inruns1, marker = 'd', markerfacecolor = 'red')   #amplitude vs zsensor
    plt.show()
```

```python
for cuva in range(0,maxima.shape[0]):
    inruns = dataarray[maxima[cuva]:minima[cuva+1],0,3]
    inruns1 = dataarray[maxima[cuva]:minima[cuva+1],0,1]
    plt.plot(-inruns, inruns1)        #amplitude vs zsensor together
    plt.savefig("amplitude vs zsensor overall.png")
plt.show()


for cuva in range(0,maxima.shape[0]):
    inruns = dataarray[maxima[cuva]:minima[cuva+1],0,3]
    inruns2 = dataarray[maxima[cuva]:minima[cuva+1],0,2]
    plt.plot(-inruns, inruns2)        #phase vs zsensor
    plt.show()


for cuva in range(0,maxima.shape[0]):
    inruns = dataarray[maxima[cuva]:minima[cuva+1],0,3]
    inruns2 = dataarray[maxima[cuva]:minima[cuva+1],0,2]
    plt.plot(-inruns, inruns2)        #phase vs zsensor together
plt.savefig("phase vs zsensor overall.png")
plt.show()


## plotting zsensor values against the user input values ##
for cuva in range(0,maxima.shape[0]):
    inruns = dataarray[maxima[cuva]:minima[cuva+1],0,3]
    inruns3 = dataarray[maxima[cuva]:minima[cuva+1],0,4]
    plt.plot(-inruns, inruns3)
plt.savefig("zsensor vs userinput.png")
plt.show()


## linear fit of the Z sensor ##
print(len(inruns), " = number of datapoints between minimum and maximum.") #same for other
parameters
x = np.arange(0,205,1)
print(x.shape)
y = inruns
print(inruns.shape)
model = LinearRegression(fit_intercept = True)
model.fit(x[:, np.newaxis], y)
yfit = model.predict(x[:, np.newaxis])
plt.scatter(x,y)
plt.plot(x,yfit)
plt.show()
print(yfit.shape)
```

```python
## plot amplitude and phase versus fitted Zsensor ##
value1 = len(inruns1) #comparing number of datapoints of x and y before plotting
print(value1)
if value1 > 205:
    inruns1 = inruns1[:-1]
else:
    inruns1=inruns1

for cuva in range(0,maxima.shape[0]):
    plt.plot(-yfit, inruns1)        #amplitude vs fit zsensor
plt.savefig("amplitude vs fit.png")
plt.show()


value2 = len(inruns2) #comparing number of datapoints of x and y before plotting
print(value2)
if value2 > 205:
    inruns2 = inruns2[:-1]
else:
    inruns2=inruns2

for cuva in range(0,maxima.shape[0]):
    plt.plot(-yfit, inruns2)        #phase vs fit zsensor
plt.savefig("phase vs fit.png")
plt.show()
```

Auteursrechtelijke overeenkomst

Ik/wij verlenen het wereldwijde auteursrecht voor de ingediende eindverhandeling:
Molecular scale insights into initial apatite growth to enhance bone regeneration

Richting: **Master of Biomedical Sciences-Bioelectronics and Nanotechnology**
Jaar: **2018**

in alle mogelijke mediaformaten, - bestaande en in de toekomst te ontwikkelen - , aan de Universiteit Hasselt.

Niet tegenstaand deze toekenning van het auteursrecht aan de Universiteit Hasselt behoud ik als auteur het recht om de eindverhandeling, - in zijn geheel of gedeeltelijk -, vrij te reproduceren, (her)publiceren of distribueren zonder de toelating te moeten verkrijgen van de Universiteit Hasselt.

Ik bevestig dat de eindverhandeling mijn origineel werk is, en dat ik het recht heb om de rechten te verlenen die in deze overeenkomst worden beschreven. Ik verklaar tevens dat de eindverhandeling, naar mijn weten, het auteursrecht van anderen niet overtreedt.

Ik verklaar tevens dat ik voor het materiaal in de eindverhandeling dat beschermd wordt door het auteursrecht, de nodige toelatingen heb verkregen zodat ik deze ook aan de Universiteit Hasselt kan overdragen en dat dit duidelijk in de tekst en inhoud van de eindverhandeling werd genotificeerd.

Universiteit Hasselt zal mij als auteur(s) van de eindverhandeling identificeren en zal geen wijzigingen aanbrengen aan de eindverhandeling, uitgezonderd deze toegelaten door deze overeenkomst.

Voor akkoord,

De Smet, Yana

Datum: **7/06/2018**